Nuclear Science and Techniques (2026) 37:37
https://doi.org/10.1007/s41365-025-01837-7

A high-accuracy particle-type labeling method for organic scintillator pulse waveform datasets

Lin-Jun Hou[1,2] · **Peng Xu**[1] · **Zhi-Meng Hu**[2] · **Jie Cheng**[3]

Received: 7 July 2024 / Revised: 25 August 2024 / Accepted: 31 August 2024 / Published online: 5 January 2026

Abstract

The pulse shape discrimination technique plays a pivotal role in neutron field measurements using organic scintillator detectors, and the particle-type labeling accuracy of the pulse waveform dataset has a significant impact on its performance, especially with the growing use of machine learning methods. In this study, a high-accuracy labeling method for pulse waveform datasets based on the time-of-flight (TOF) filtering method, an improved charge comparison method (CCM), and the coincidence measurement method is proposed. The relationship between the experimental parameters and the chance coincidence proportion in the TOF measurement was derived to reduce contamination from chance coincidences at the experimental level. Based on this, an experiment was conducted to obtain raw data using the ^{241}AmBe source, and a piled-up identification algorithm based on reference waveform cross-correlation and differential analysis was designed to filter out piled-up pulses. To improve the labeling accuracy, the CCM was optimized, a simple method of selecting the TOF interval for a lower chance coincidence proportion was proposed, and a low-amplitude pulse waveform dataset construction method based on coincidence measurements was developed. To verify these methods, eight pulse waveform datasets were constructed using different combinations of the proposed approaches. Three neural network structures and a corresponding evaluation parameter were designed to test the quality of these datasets. The results showed that the particle identification performance of the CCM was significantly improved after optimization, with the neutron-to-gamma-ray misidentification rate reduced by more than 35%. The proposed accuracy improvement methods reduced ambiguous identification results from these artificial neural networks by more than 50%.

Keywords Pulse shape discrimination · Organic liquid scintillator · Time of flight · Charge comparison method · Machine learning

1 Introduction

When a neutron is emitted from or captured by an atomic nucleus, the nucleus is generally in an excited state that is unstable and tends to be de-excited by emitting gamma-rays. As a result, nearly all neutron fields inevitably contain gamma radiation, making the suppression of this interference is a vital issue in neutron field measurements. In general, there are three approaches to mitigating gamma radiation interference: Material selection—Using detection materials inherently insensitive to gamma-rays, such as ^{238}U [1–3] or ^{6}Li [4, 5]; the time-of-flight (TOF) method can particles by their velocities to filter out gamma-rays. Pulse shape discrimination (PSD)—Identifying particle types by analyzing differences in pulse shapes. Organic liquid scintillator (OLS) detectors are widely used for neutron field

---

This work was supported by the National Natural Science Foundation of China (Nos. 12375297 and 12105144).

✉ Peng Xu
xupeng76345@163.com

✉ Zhi-Meng Hu
huzhm21@nuaa.edu.cn

[1] PLA Rocket Force University of Engineering, Xi'an 710025, China

[2] Department of Nuclear Science & Engineering, Nanjing University of Aeronautics and Astronautics, Nanjing 210016, China

[3] Institute of Nuclear Energy Safety Technology, Hefei Institutes of Physical Science, Chinese Academy of Sciences, Hefei 230031, China

measurements, including fusion reactor diagnostics [6–9] and the non-destructive testing of special nuclear materials [10, 11]. Although OLS detectors are sensitive to both neutrons and gamma-rays, the waveforms they produce differ between particle types, enabling PSD-based discrimination. The fluorescence decay time constants of OLS, as well as the fluorescence yield ratio between components with different decay constants, are influenced by various external factors. Of particular importance is the particle's linear energy transfer (LET), which strongly affects the transition of *pi* electrons from the T1 state to the S1 state. This is due to the significant role played by short-range two-body interactions in the process [12]. Neutrons and gamma-rays deposit energy indirectly: Neutrons primarily through recoil protons generated by np scattering, and gamma-rays through recoil electrons produced by Compton scattering. Because of the large mass difference between electrons and protons, their LET values differ substantially for particles of similar energy. Consequently, the pulse shapes produced by neutrons and gamma-rays differ in measurable ways, allowing particle identification through pulse waveform analysis.

The most established and widely used PSD algorithm is the charge comparison method (CCM), which remains prevalent even in the era of digital signal processing owing to its high accuracy and low computational complexity [13–15]. With advances in deep learning, attention has shifted toward artificial neural network-based discrimination algorithms, which can achieve higher particle-type identification accuracy with only a negligible increase in computational complexity [16–19]. Pulse waveform datasets are essential in the design of PSD algorithms, and the accuracy of particle-type labels is critical for both parameter optimization and performance evaluation. In most existing studies, datasets for training and testing supervised machine learning algorithms are generated using PSD methods such as CCM [20–23], and lead or polyethylene bricks may be used to shield unwanted radiation to achieve higher label accuracy [24]. However, the limited ability of current algorithms to correctly classify low-amplitude pulses constrains the accuracy of labels produced by these methods, making them unsuitable for robust algorithm training and testing. Additionally, owing to the strong ability of machine learning algorithms to fit ordinary computational models, they approximate the CCM when trained on datasets generated by the CCM, which should be avoided.

In recent years, some studies have adopted the TOF method to generate pulse waveform datasets, which has greatly improved labeling accuracy. However, owing to chance coincidence, it is still necessary to apply optimization methods to further improve the labeling accuracy. Lennox et al. proposed selecting the TOF interval with the lowest number of chance coincidence counts [25]. David Fobar et al. refined TOF datasets using the CCM [26]. Hachem et al. applied the CCM to filter chance coincidence events and verified the dataset production method using a simple neural network [27]. While these approaches combine traditional techniques with TOF to improve particle-type labeling accuracy, opportunities for further refinement remain. For example, a quantitative analysis of the factors influencing the proportion of chance coincidence counts could be used to optimize experimental parameters and reduce such coincidences at the experimental level. Further optimization of the CCM can significantly improve its filtering effect in the TOF data processing, and because the existing PSD algorithms are less effective in discriminating low-amplitude pulses, and because TOF data have a higher percentage of chance coincidence in the low-amplitude range due to the presence of background radiation, focused attention is needed to improve the particle-type labeling accuracy of the low-amplitude portion of the dataset.

To further improve the particle-type labeling accuracy of the pulse waveform dataset, a high-accuracy labeling strategy based on the optimized CCM, TOF method, and coincidence measurement method was proposed in this study. The structure of this study was divided according to the logic of the method. Section 2 details the raw data acquisition and preprocessing methods by which single-pulse waveforms and their TOF can be obtained. First, the experimental principle is outlined, and the quantitative relationship between the ratio of true-to-chance coincidences and the experimental parameters is derived. A piled-up pulse identification algorithm, based on reference waveform cross-correlation and differential analysis, is then introduced to remove piled-up pulses. Section 3 presents and validates three methods to improve particle-type labeling accuracy. First, the optimal short and long integration gates and the discrimination threshold of the CCM are determined for different pulse amplitudes to enhance discrimination performance. A simple method to determine the time interval that can filter out the largest proportion of chance coincidence for different pulse amplitudes is proposed, and a coincidence measurement method for the high-accuracy labeling of low-amplitude pulse waveforms is designed. To verify these methods, three neural networks with different structures were designed, and eight datasets obtained using different combinations of these methods were generated and fed into the networks. Finally, a classification effect evaluation parameter was designed to test these networks. Finally, Sect. 4 concludes the paper.

2 ToF experiment and data preprocessing

2.1 Experimental principles and settings

The most critical issue in TOF measurement experiments is the acquisition of the start time. The most widely used neutron sources in this type of research are ^{252}Cf and ^{241}AmBe neutron sources, which produce neutrons through spontaneous nuclear fission and nuclear reactions, respectively, accompanied by associated gamma radiation. In this study, an AmBe source was used. AmBe neutron sources are typically fabricated by grinding, mixing, and then compression-molding Am oxides with Be or by directly melting and casting Am and Be into an alloy. ^{9}Be is a stable nuclide, and ^{241}Am has a long half-life of approximately 432.6 years. Therefore, AmBe neutron sources have the advantages of stability in key parameters and lower cost, and are widely used. AmBe sources primarily produce neutrons through a $^{9}\mathrm{Be}(\alpha,\mathrm{n})^{12}\mathrm{C}^{*} \rightarrow \gamma(4.438\,\mathrm{MeV})$ reaction, and the actual neutron yield per million alpha particles is approximately 60–74 [28]. The lifetime of C* in this reaction is 6.1×10^{-14} s [29], which is significantly smaller than the detector time resolution and neutron flight time. Therefore, prompt gamma-rays can be used to mark the neutron emission time and realize neutron TOF measurements.

To reduce chance coincidence in the TOF measurement experiment, a quantitative relationship between the ratio of true to chance coincidence and the experimental parameters should be derived. The ratio of true coincidence to chance coincidence can be expressed as:

$$R(t_1,t_2) = \frac{Nk_1k_2Q(t_1,t_2)}{(Nk_1+b_1)(Nk_2+b_2)(t_2-t_1)}, \tag{1}$$

where N is the neutron source strength, k_1 and k_2 are the total detection efficiencies of detector 1 (closer to the source) and detector 2, respectively, b_1 and b_2 are background counting rates, t_1 and t_2 specify the interval of TOF, and $Q(t_1,t_2)$ is a composite coefficient whose product with k_2 is the probability that detector 2 detects a particle in the time interval (t_0+t_1, t_0+t_2) under the condition that detector 1 has detected one or more of the associated particles at t_0. In general, Nk_1 is much larger than b_1. Therefore, the equation can be reduced to

$$R(t_1,t_2) = \frac{k_2}{Nk_2+b_2}q(t_1,t_2), \tag{2}$$

where $q(t_1,t_2) = Q(t_1,t_2)/(t_2-t_1)$, which is related only to the spectrum and multiplicity of the source, and is not affected by other general settings. According to this formula, there are four methods to increase the proportion of true coincidences: 1. Choose a neutron source with appropriate activity according to the background count rate; 2. use shielding for detector 2 to shield the background radiation (which may activate gamma radiation); 3. reduce the distance between detector 2 and the source to increase k_2 appropriately while maintaining sufficient time resolution; and 4. select the appropriate TOF interval (t_1,t_2) to increase q by as much as possible.

The neutron source used in our TOF measurement experiment was the AmBe source at the Institute of Heavy Ion Physics, Peking University, with a neutron emission rate of $1.08 \times 10^{6}\ \mathrm{s}^{-1}$ and an approximate ratio of 0.573 between the emission rates of SI 4.438 MeV gamma-rays and neutrons [30]. A schematic diagram and the experimental site layout are shown in Fig. 1. Detector A was an EJ-301 organic liquid scintillator coupled to an ET 9814KB photomultiplier tube, which was housed in an elaborately designed composite shield to minimize background counts. Detector B was a BC-501A organic liquid scintillator coupled to a Hamamatsu R329-02 photomultiplier tube, which was closer to the AmBe source. Both EJ-301 and BC-501A are commercial equivalents of NE-213 produced by different companies and exhibit the best PSD performance among liquid scintillators. Two scintillators used in this experiment had a 2-inch diameter and were housed in bubble-free cells to minimize temperature-related effects. The detectors were powered by an ISEG SHR high-precision high-voltage supply at 1550 V. Analog signals from the photomultiplier tube voltage dividers were digitized by a CAEN DT5751 desktop digitizer at a sampling rate of 1 GS/s with 10-bit resolution. The dynamic ranges of the input voltage and digitizer impedance were 1 V

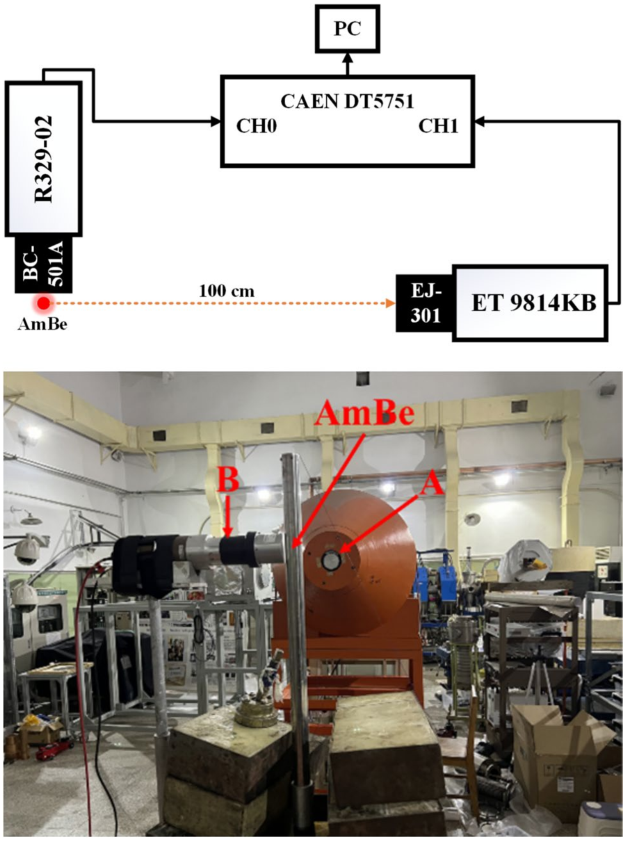

Fig. 1 (Color online) The schematic diagram and the site layout of the experiment

and 50 Ω, respectively. The digitizer communicated with the CoMPASS software on a PC via USB, and the waveforms, along with their corresponding trigger times, were stored in CERN ROOT format.

2.2 Piled-up filtering

To exclude the interference of the piled-up pulses, piled-up filtering must first be performed. We propose a piled-up discrimination algorithm that combines reference waveform cross-correlation and differential analysis methods to identify piled-up pulses. The exact steps are:

1. Fit the average waveform of the pulses measured under low count rate condition with the double exponential decay model [12], in which the change rate of the number of off-domain π-electrons in the S1 energy state can be expressed by:

   $$\frac{\mathrm{d}N}{\mathrm{d}t} = H\frac{e^{-t/t_\mathrm{r}}}{t_\mathrm{r}} - \frac{NA}{t_\mathrm{f}} - \frac{N(1-A)}{t_\mathrm{s}}, \tag{3}$$

   where N characterizes the total excitation, t_r, t_f, and t_s denote the rise time, fast and slow decay time constants, respectively, and A denotes the ratio of fast to total components. The rise time is primarily influenced by the transfer efficiency of excitation energy from the solvent to the solute. The fast decay time mainly depends on the lifetime of the S1 energy state of the π-electrons, whereas the slow decay time mainly depends on the efficiency of the conversion of the π-electrons from the T1 energy state to the S1 energy state. The emission rate of the fluorescence photons can be expressed by the absolute value of the last two terms of this formula, which describes an unbroadened waveform, and the real pulse waveform can be obtained by Gaussian broadening. According to this model, the reference pulse waveform, expressed by $x = [x_1, x_2, \cdots, x_m]$, can be obtained through numerical fitting;
2. Calculate the cross-correlation vector c between the reference pulse waveform x and the measured waveform y, where $c = [c_1, c_2, \cdots, c_{n-m+1}]$, $y = [y_1, y_2, \cdots, y_n]$(baseline channel minus sample channels for negative signal), and $c_i = \sum_{k=1}^{m} x_k y_{i+k-1}$;
3. Differentiate and double differentiate c, and then get the number of pulses by conditional judgment.

This method significantly enhanced the algorithm's ability to discriminate between noise and signal by incorporating a reference waveform cross-correlation operation, thereby overcoming the poor noise immunity of the simple differential method. As shown in Fig. 2, Fig. 2(a) is the raw waveform of the piled-up pulses, Fig. 2(b) is the cross-correlation vector **c**, and Fig. 2(c) and (d) are the differential and double-differential curves of **c**, respectively. This shows that after the cross-correlation and differentiation operations, the number of pulses becomes more distinct and can be readily determined through differential analysis and conditional judgment.

3 Methods for labeling accuracy improving

3.1 Optimization of charge comparison method

The CCM is the most widely used PSD algorithm. It quantifies the difference in the proportions of fluorescence components with different decay time constants between the pulse waveforms of various particle types by comparing the ratios of charge integrals over different time intervals. The PSD parameter P is calculated as:$P = \sum_{i=1}^{pp+s} h_i / \sum_{i=1}^{pp+l} h_i$. As shown in Fig. 3, pp, s, and l are the prepeak, short-, and long-term integral gates of the charge integral, respectively. In this study, pp had a fixed value of 25. $s < l$, h_i is the gap between the values of sample i and the baseline, and P should be compared with the threshold Th. Th is an artificially selected threshold used for comparison with the PSD parameters to achieve classification. For example, in a bimodal Gaussian distribution, Th can be selected at the intersection of two peaks. If $P < Th$, the particle is more likely to be a neutron with a slower fluorescence component.

Traditional CCM uses fixed integration gates and discrimination thresholds. In practice, however, the signal-to-noise ratio (SNR) changes over time in different ways for pulses of different amplitudes. A long gate that is too large results in an increase in the noise proportion, whereas a long gate that is too small cannot make full use of the information in the pulse waveform. Similarly, a short gate has an optimal value that changes with the pulse amplitude. Furthermore, because the linear energy transfers of protons and electrons differ with energy, the ratio of fast to slow fluorescence components also changes. Figure 4 shows the scatter density map of the discrimination parameters for the measured pulse waveform data from the AmBe source with $l = 100$ and $s = 15$. PH refers to the pulse amplitude, and the unit MeVee means MeV electron equivalent. It can be observed that the optimal discrimination threshold changes with the pulse amplitude, which is more evident in the low-energy regions. In summary, it is necessary to determine the optimal values of the three key CCM parameters, s, l, and Th for pulses with varying amplitudes to enhance the PSD capability of the CCM.

As an optimization problem, the key challenge lies in designing an effective evaluation method and optimization strategy. A traversal method is used to determine the optimal CCM parameters. The discrimination performance was

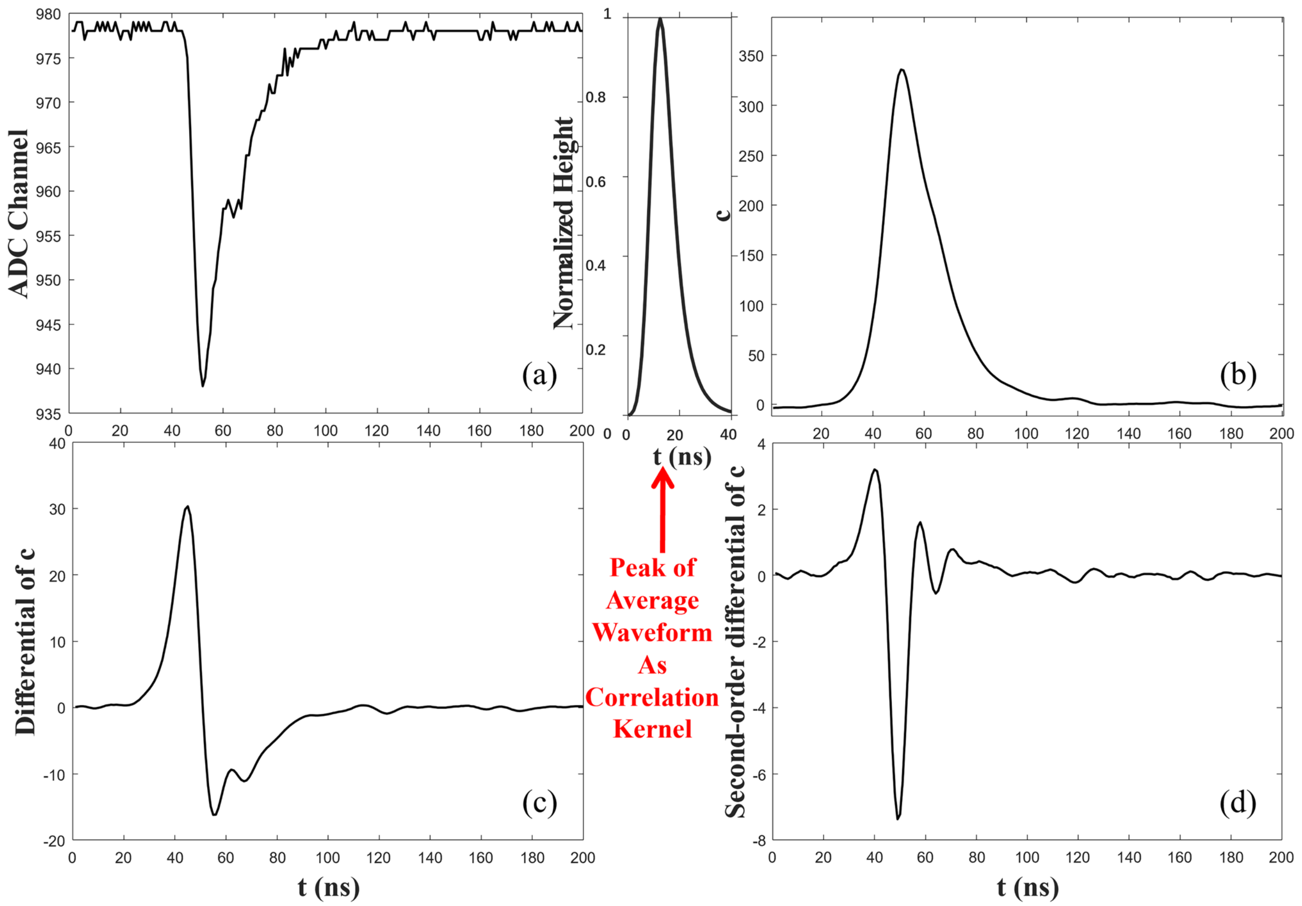

Fig. 2 (Color online) Waveforms in piled-up filtering process. **a** is the raw measured waveform, **b** is the cross-correlation waveform, and **c** and **d** are the differential and double-differential waveforms

quantified by the degree of separation between the two categories formed by the PSD parameters. A double-Gaussian fitting method was used to evaluate the discrimination effect. After fitting the frequency distribution curve of the PSD parameters to the double-Gaussian model, the discrimination effect can be expressed as

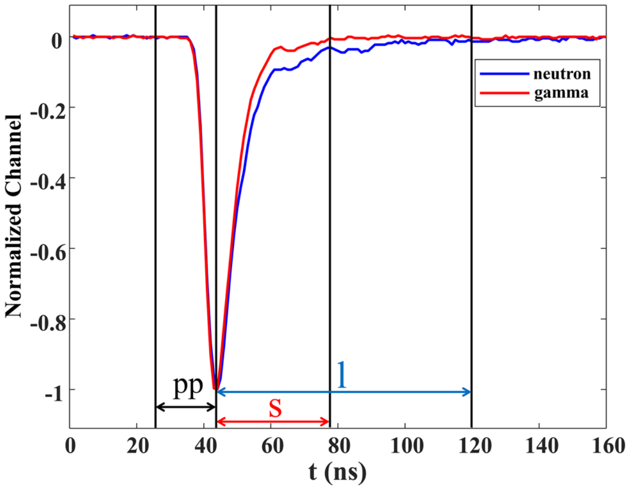

Fig. 3 (Color online) Schematic diagram of the CCM

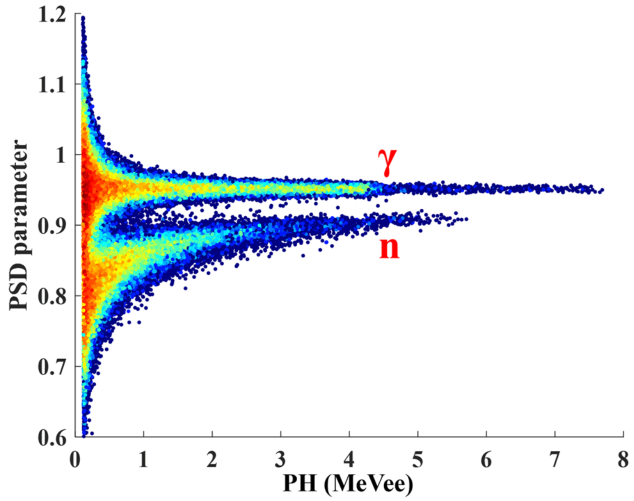

Fig. 4 (Color online) Scatter density map of the CCM PSD parameters for AmBe source

$$D = \frac{|\mu_1 - \mu_2|}{\sigma_1 + \sigma_2},$$

where μ_1, μ_2, σ_1 and σ_2 are the means and standard deviations of the two Gaussian curves, respectively. A larger D indicates less overlap between the two Gaussian distributions, a lower misclassification rate, and thus a better set of CCM parameters. Theoretically, this evaluation method allows us to obtain the optimal parameters through a traversal search with a suitable step size. However, the convergence of the double-Gaussian fitting can be unstable due to local optima or overfitting, which significantly affects the optimization results. We performed the fitting using the SciPy.optimize module (v1.13.0), with nonlinear least squares solved iteratively via the Trust Region algorithm [31] and random initial values. In practice, the random initialization method proved highly unstable when discrimination was poor. As shown in Fig. 5a, the evaluation parameter D varied sharply and irregularly with s and l in the low-D region, underscoring the importance of improving the stability of the double-Gaussian fitting, particularly for low-amplitude pulses.

To improve the stability of the fitting, it is important to determine a better boundary and initial point for double-Gaussian fitting. We propose a two-sided pre-fitting approach. The core idea is to first perform single-Gaussian fitting on each side of the distribution separately, and then use the results from these two fits to establish both the initial parameter estimates and the reference boundaries for the subsequent double-Gaussian fitting. The procedure is as follows.

1. Normalize and differentiate the frequency distribution curve of the PSD parameters. From each side of the curve, identify the first point whose absolute differential value exceeds a predefined threshold. The threshold is set proportionally to the peak value on the corresponding side. These points serve as the starting positions for data selection in the pre-fitting stage;
2. From each identified starting point, select N consecutive points moving toward the center of the curve and fit each segment independently with a single-Gaussian model; N is negatively correlated with the maximum differential value of the curve (a larger maximum differential value indicates that the curve is high and thin, and can be fitted with fewer data points, whereas too many data points will contaminate the fit);
3. Use the results of the two-sided pre-fitting to set the boundaries and initial values of the parameters for the double-Gaussian fitting and obtain a more stable fitting result.

As shown in Fig. 5b, compared with the random initial value method, the two-sided pre-fitting method can significantly improve the stability of the fitting results. Therefore, using this evaluation method, the optimal long- and short-time-integral gates can be determined using the ergodic method, and the fitting result of the PSD curve obtained using these optimal integration gates can then be fitted to derive the corresponding optimal discrimination thresholds.

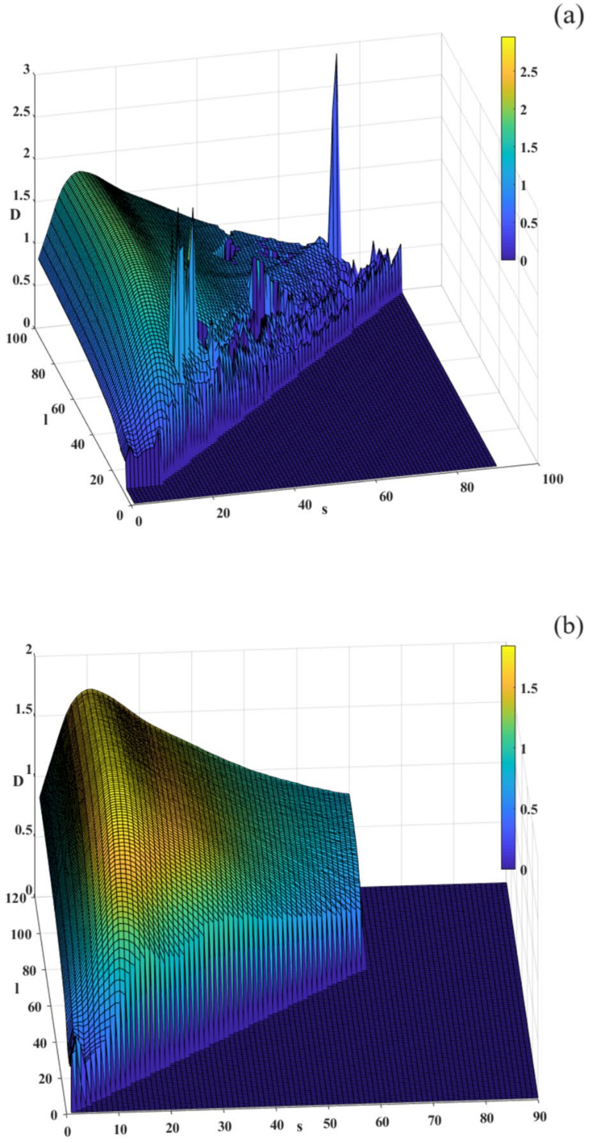

Fig. 5 (Color online) Map of fitting results for the random initialization method **a** and the two-sided pre-fitting initialization method **b**, where the region of no interest is ignored to save computational resources

The frequency distribution curves of the PSD parameters for the pulses with different energy ranges are shown in Fig. 6, and the top and bottom three figures show the results of the original and optimized CCM, respectively. A clear improvement in PSD performance is observed after

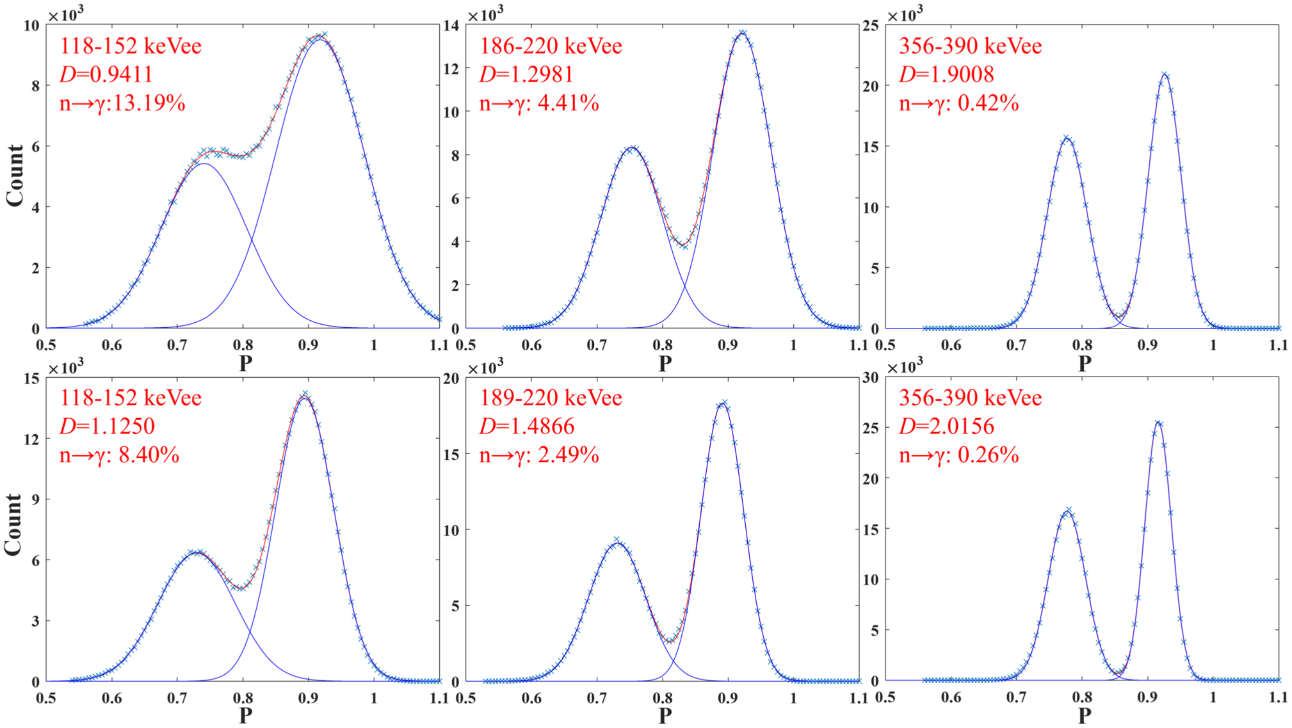

Fig. 6 (Color online) Frequency distribution curves of the PSD parameters for different pulse heights. The top and bottom three are the results of the original and optimized CCM, respectively

optimization. Specifically, for pulses in the ranges 118–152 keVee, 186–220 keVee, and 356–390 keVee, the fraction of the left Gaussian integral lying to the right of the threshold, representing the probability of a neutron being misidentified as a gamma-ray—decreases from 13.19%, 4.41%, and 0.42% in the original CCM to 8.40%, 2.49%, and 0.26%, respectively, in the optimized CCM. For pulses above 0.356 MeVee, the discrimination metric *D* exceeds 2.01, indicating negligible overlap between the two Gaussian peaks. This implies that, post-optimization, the CCM achieves reliable neutron–gamma discrimination for pulses above 0.356 MeVee. It is important to note that the gain of the photomultiplier tube and the dynamic range and resolution of the ADC system have a significant impact on the signal-to-noise ratio of the signal in the low-energy region, which, in turn, affects the relationship between the energy range and the discrimination effect. For the -1550 V voltage used in our experiment, the peak height of the 0.356 MeVee pulse is approximately 39 LSB (Least Significant Bit), which is less than 4% of the range.

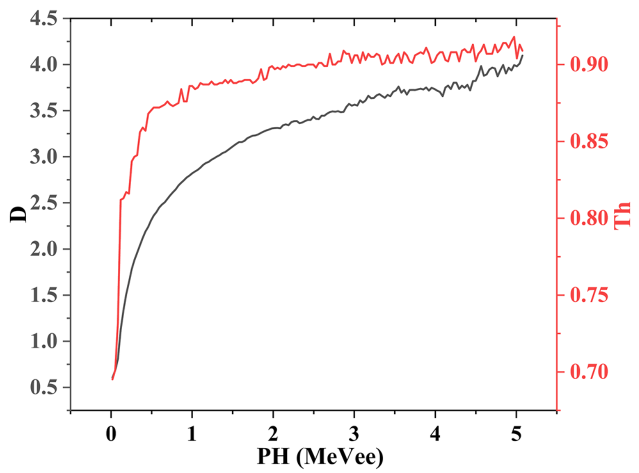

Fig. 7 (Color online) Optimal *D* and *Th* for different pulse heights

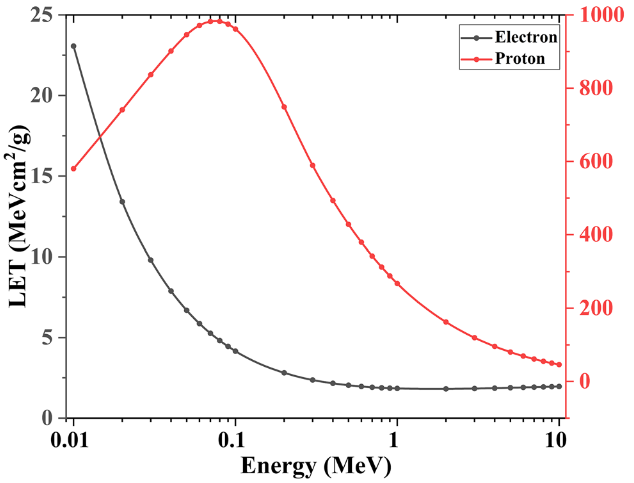

Fig. 8 (Color online) LET of protons and electrons in xylene

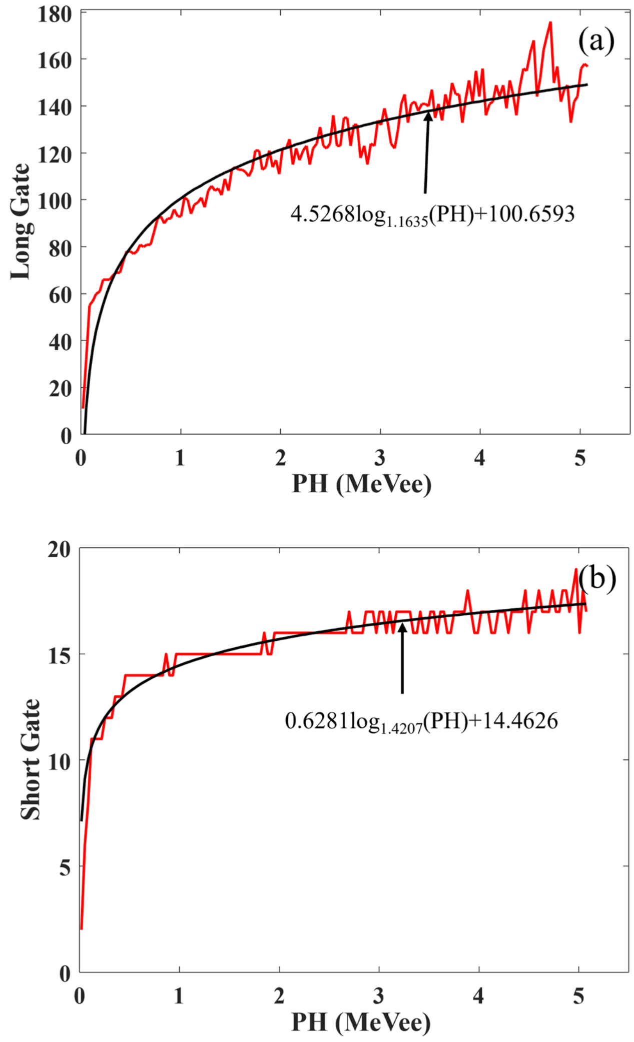

Fig. 9 (Color online) Optimal long **a** and short **b** gates for different pulse heights

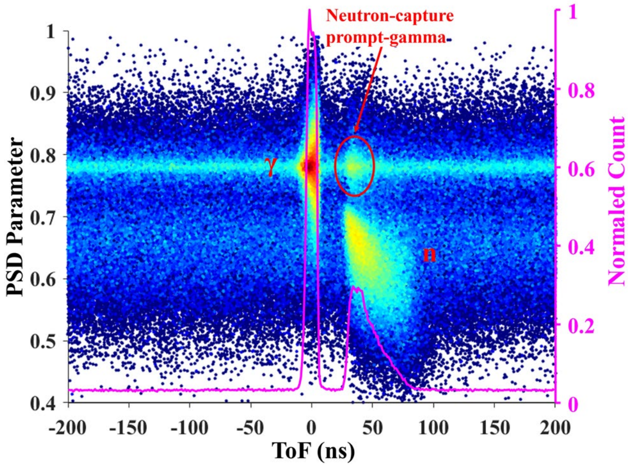

Fig. 10 (Color online) Scatter density plot of CCM PSD parameters versus TOF. For the two parallel bright areas, the upper one is for gamma-rays, and the lower one is for neutrons. The magenta curve is the TOF distribution curve

As shown in Fig. 7, the discrimination effect increases with pulse height, and the fluctuation and slope at the end of the curve are due to the insufficient sample size at high pulse heights. The optimal discrimination thresholds for pulses with different heights are shown in Fig. 7. It can be seen that the threshold increases with the pulse height roughly, which is consistent with the physical law. The linear energy transfers for different energies of protons and electrons in xylene were calculated using a Monte Carlo simulation with Geant4 v11.2.1 [32–34] and are shown in Fig. 8. For protons and electrons with energies above 100 keV, LET decreases with increasing energy. Thus, as discussed in the introduction, the proportion of the fast component in radioluminescence increases with particle energy, as does the threshold. In addition, although we did not study pulses with a pulse height greater than 5.1 MeVee owing to the insufficient sample size, the optimal thresholds at the right end are also applicable, as the discrimination effect of the algorithm is sufficient for high-amplitude pulses. The optimal long- and short-term integral gates for pulses with different heights are shown in Fig. 9. As the pulse amplitude increased, the optimal time-integral gates increased, whereas the growth rate decreased gradually. Therefore, we fitted this curve to a logarithmic model, and the results are shown in Fig. 9. The improvement effect of our optimization method on the discrimination effect of the CCM is clearly shown in the next subsection.

3.2 Optimal time interval for TOF filtering

The main concept of our pulse waveform dataset production method is the combination of TOF and PSD filtering to minimize the error labels of the particle type. The TOF distribution is shown by the magenta curve in Fig. 10, and the scatter density map of the relationship between the CCM PSD parameters and TOF is shown in this figure. There are two bright lines in the density map (the upper and obvious lines represent gamma-rays, and the lower and obscure lines represent neutrons) parallel to the ToF axis, indicating that chance coincidence cannot be ignored. Therefore, it was necessary to use the PSD method to purify the TOF data. The TOF curves of the four different PSD cases ($\gamma\gamma$, nγ, γn, and nn, where nγ indicates that, in a coincidence event, the pulse obtained by the detector closer to the source is identified as a neutron signal, whereas the pulse obtained by the other detector is identified as a gamma signal by the PSD algorithm) are shown in Fig. 11. Figure 11a shows the original CCM, and Fig. 11b shows the optimized CCM. In both cases, the pulse height threshold was set to 100 keVee. It can be seen that for the result of the original CCM, there are

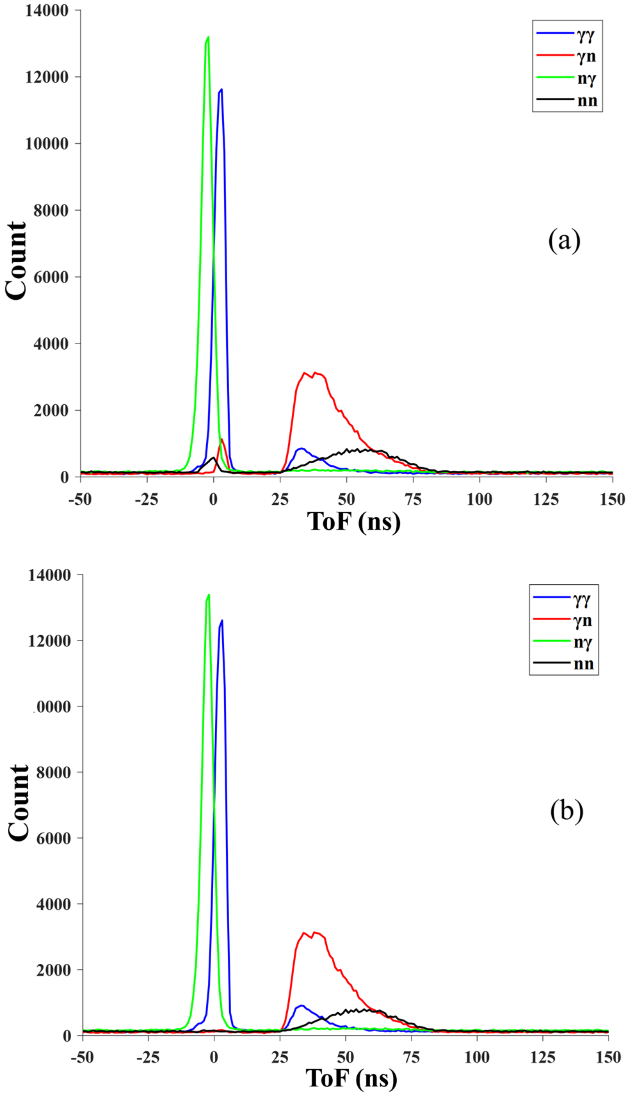

Fig. 11 (Color online) ToF counts distribution curves classified by original CCM **a** and optimized CCM **b**

unwanted peaks of nn and γn coincidence around the zero ToF, indicating that there is a considerable amount of false discrimination for low-amplitude pulses. For the optimized CCM, these false discrimination peaks disappeared, clearly demonstrating the PSD performance improvement effect of the optimization. In addition, there is a $\gamma\gamma$ peak on the right side, which can also be observed in Fig. 10 as the bright circled area on the upper right, which cannot be removed by increasing the threshold or using the PSD method. This $\gamma\gamma$ peak is caused by prompt gamma-rays emitted by neutron-activated nuclei, which means that the use of a shield may have a negative effect on the dataset production. This is an important reference for the experimental design.

To label the pulses as accurately as possible; after optimizing the PSD method, it is crucial to develop a strategy to find the optimal time interval for the TOF filtering of different pulse amplitudes. Because of the difficulty in accurately obtaining the error rate of the PSD method, we did not consider the correlation factor between the TOF and particle-type discrimination accuracy of the PSD algorithm when developing our time-interval selection strategy. However, based on the qualitative analysis, this would not significantly impact on our study. Accordingly, because the count of chance coincidence was uniformly distributed along the TOF axis, we only needed to determine the corresponding optimal TOF intervals at which the neutron counts for different pulse amplitudes reached their maxima. For neutrons of energy below 20 MeV, the differential cross-section of the ^{1}H(n, n)^{1}H scattering is nearly isotropic in the center-of-mass reference system [35], and the energy of the recoil protons obeys a uniform distribution from 0 to the neutron energy according to the elastic scattering. Based on this, the neutron count distribution over the TOF versus the recoil proton energy can be calculated by numerically integrating the TOF data of γn coincidence, as shown in Fig. 12. According to this count distribution map, the optimal TOF interval for different pulse heights can be obtained, which can help purify the pulse waveform data.

3.3 Optimization method for low-amplitude data

Existing PSD methods are not effective for high-accuracy discrimination of pulses with amplitudes below 200 keVee (affected by the gain characterization and digitizing resolution of the detector). Consequently, the promoting effect of these methods on the particle-type labeling accuracy of the pulse waveform dataset obtained by TOF filtering of AmBe source measurement data in this amplitude range is not sufficient. In addition, because the pulse amplitudes were mainly concentrated in the low-amplitude region in TOF measurements, the proportion of chance coincidences was higher in this region. Therefore, it is necessary to design a method to improve the particle-type labeling accuracy in low-amplitude regions. In this study, experimental strategies for coincidence measurements were designed to purify a low-amplitude waveform dataset. In the case of gamma pulses, the most straightforward approach is to individually measure the gamma source. A coincidence measurement method can be used to eliminate the background neutron interference. As shown in Fig. 13a, the two detectors are placed 5 cm facing each other and a 4.6 $\times 10^4$ Bq ^{137}Cs source is attached to the EJ-301 detector. The gamma-rays from the ^{137}Cs source are monoenergetic with an energy of 661.657 keV, and they mainly undergo Compton scattering in OLS according to the photon–matter interaction. When a scattered gamma-ray is detected by another detector, a coincidence event can be obtained. The background neutron interference was suppressed by reducing the coincidence time window. Additionally, the Compton electron energy limit and

Fig. 12 (Color online) Neutron count distribution over the TOF versus the recoil proton energy

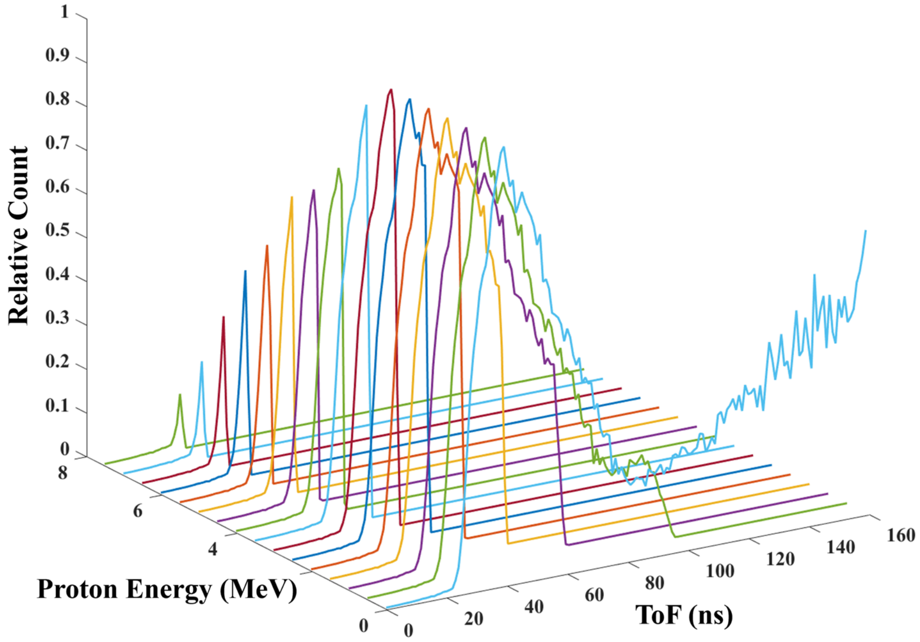

an optimized CCM with a biased threshold—set lower than the standard discrimination threshold to minimize gamma-to-neutron misclassification—were applied to exclude residual neutron signals. Gamma sources that emit correlated gamma-rays, such as ^{60}Co, were deliberately avoided. This is because the scattered gamma-ray and its correlated partner can produce Compton electrons in the same detector almost simultaneously, causing waveform distortion due to differences in the LET of electrons at different energies.

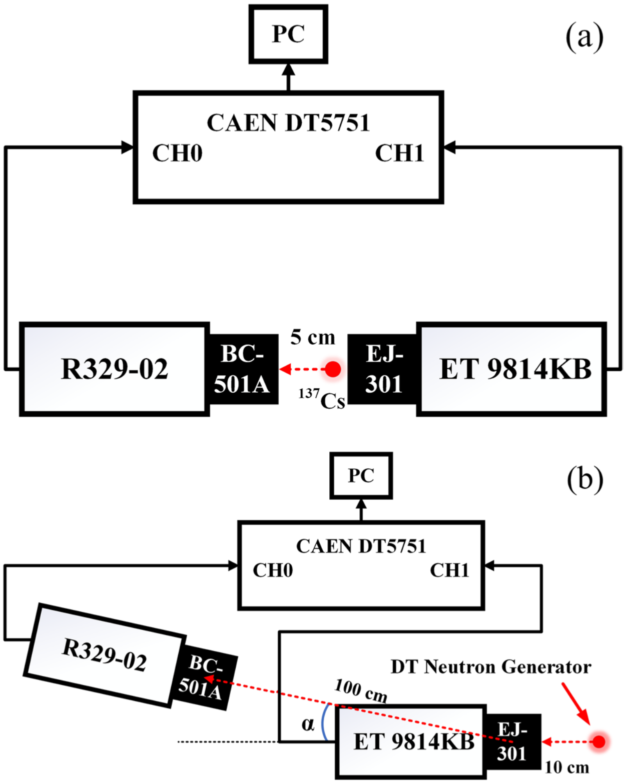

Fig. 13 (Color online) The schematic diagram for gamma **a** and neutron **b** coincidence measurement

The coincidence method can also be used for the low-amplitude neutron pulse waveform data. As shown in Fig. 13b, the EJ-301 detector was placed facing the DT neutron generator at a distance of 10 cm, and the BC-501A detector was placed 1 m behind it at an angle α to the axis. The 14.08 MeV neutron was emitted by the DT neutron generator and then scattered in the EJ-301 OLS, and if the scattered neutron was detected by the other detector, a coincidence event would be obtained. In this scattering geometry, both the scattering angle and the energy of the incident neutron are known, and the energies of the recoil proton and scattered neutron can be calculated using elastic scattering equations. Based on this, the pulse amplitude, TOF, and optimized CCM with a biased threshold (smaller than the normal discrimination threshold to reduce the gamma-to-neutron probability) could be precisely controlled by adjusting the scattering angle α, in accordance with the proton light yield curve of the EJ-301 OLS.

3.4 Evaluation of labeling accuracy improving methods

To assess the effectiveness of the methods proposed in the previous section for improving particle-type labeling accuracy in pulse waveform dataset construction, eight datasets were prepared using different method combinations. The first one was constructed only by the original CCM, the second one was constructed using the original CCM and the low-amplitude dataset improving method introduced in Sect. 3.3, the third one was constructed by the original CCM and the TOF filtering method, the fourth one was constructed by all three improving methods, and the remaining four datasets corresponded to the first four datasets with the CCM optimized. To evaluate the performances of these datasets, three classification networks were designed, the structures of which are shown in Fig. 14 (the ReLU activation functions for some of the middle layers are not shown owing to space constraints). The first network is a fully connected neural network (multilayer perceptron) with three linear layers, simple in structure, fast to train, but with limited generalization capability. The second is a simple convolutional neural network (CNN), which benefits from greater depth and improved generalization but is more prone to gradient vanishing/exploding during training. The third is a CNN incorporating Inception modules [36], which mitigates gradient problems while maintaining depth and offers more flexible convolution kernels for enhanced generalization. The BatchNorm [37] and dropout [38] methods were used to improve the training effect of these CNNs. We used the PyTorch 2.2.0 framework to build and train our networks, and the cross-entropy function was used as the loss function.

It can be assumed that the higher the particle-type labeling accuracy of the training dataset, the more effective the resulting network will be for particle identification. Because the exact particle types of the pulses cannot be known, the true or false rates are not appropriate as the norm for our network testing. Therefore, it is necessary to design an alternative evaluation method. Given that the network performs binary classification and the output layer uses a two-channel softmax activation, we assume that a larger difference between the outputs of the two channels corresponds to a more confident and effective classification. By the properties of the softmax function, the two-channel outputs sum to 1, and their difference lies in the range $(-1, 1)$. Based on this, we constructed a test set of 1 million pulse waveforms from an AmBe source and evaluated network performance by counting the number of pulses for which the output channel difference falls within $(-k, k)$, where k is a chosen threshold, and $0 < k \leqslant 1$). A smaller count indicates better discrimination performance.

Considering the randomness of the network training convergence results, we conducted 30 training sessions for each case, which showed that the network training results were stable, with a relative standard deviation below 2%. Additionally, we found that the difference between the results of the three networks was negligible (i.e., less than the standard deviation). Therefore, only the results of the multilayer perception network are shown in Fig. 15, which shows the relationship between the mean count and the threshold k. It can be seen that the optimization method proposed in this study for the CCM is very effective, and the evaluation parameters of the dataset produced using the optimized CCM are significantly reduced. Both the TOF method and low-amplitude pulse coincidence measurement method can effectively improve the performance of the dataset. When the performance of the PSD method is poor, the TOF method can significantly filter out mislabeling and improve the performance of the dataset. When using the improved PSD method, which has a better discrimination performance, the low-amplitude pulse coincidence measurement method can improve the performance of the dataset significantly than the TOF filtering method. The evaluation parameter curves of different networks trained on the same dataset overlap almost exactly, indicating that the conventional shallow fully connected neural network can perform the task of non-piled-up n/γ PSD very well, and deeper convolutional neural networks cannot further improve the network performance in this task. However, it remains possible that deeper CNNs

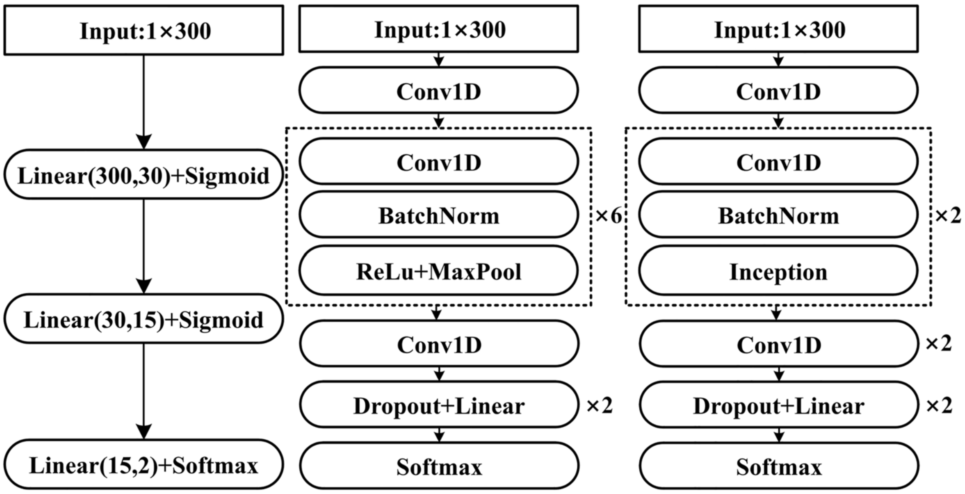

Fig. 14 (Color online) Structure diagrams of the neural networks

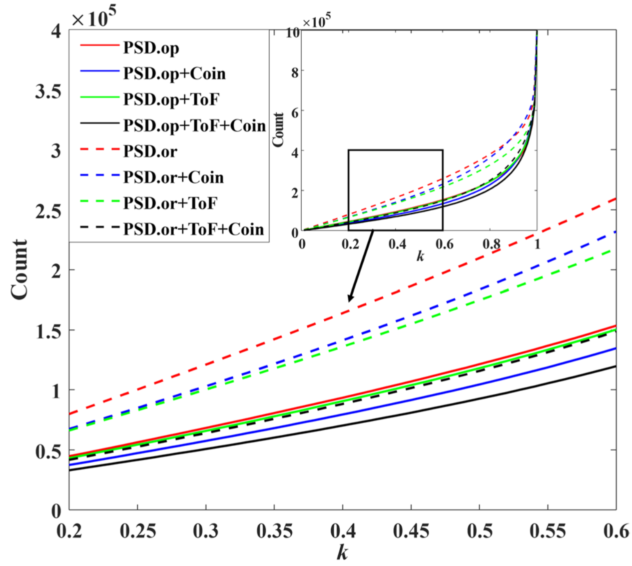

Fig. 15 (Color online) Performance test results of the multilayer perception network trained on different datasets. The vertical coordinate is the number of the pulses where the difference between the two output channels is in the range of $(-k, k)$

could outperform the MLP in more complex scenarios, such as particle discrimination involving piled-up signals and extraction of time-amplitude information.

4 Conclusion

A pulsed waveform dataset with high-accuracy particle-type labels is extremely important for the development of PSD methods. In this study, a particle-type labeling method for the OLS pulse waveform dataset based on TOF measurements and CCM PSD was proposed, and three optimization methods to improve labeling accuracy were designed and tested. The results show that: The proposed CCM optimization significantly enhances particle-type identification, and for pulses whose peak heights are about 13 LSB, 20 LSB, and 39 LSB, the probabilities of misidentifying a neutron as a gamma-ray have been reduced by 36.3%, 43.5%, and 38.1%, respectively. The low-amplitude pulse coincidence measurement method markedly improves dataset quality by replacing low-amplitude pulse data from CCM and TOF filtering. The proposed evaluation parameter provides a more convincing measure of network performance than the conventional correct identification rate. A shallow fully connected neural network is sufficient for non-piled-up n/γ PSD tasks; more complex network architecture do not architectures do not yield additional performance gains in this context. Background shields may introduce prompt activation gamma radiation, which can degrade dataset quality. In conclusion, the high-accuracy particle-type labeling method proposed in this study can significantly improve the performance of pulsed waveform datasets, which is of great importance for the development of PSD algorithms. In addition, the piled-up signal identification algorithm, the optimized CCM approach, and the proposed evaluation metric have broader applicability for other pulse signal processing and classification network evaluation tasks.

Acknowledgements The authors thank Yun-He Li (Institute of Heavy Ion Physics of Peking University) for his help in experiment preparation.

Author Contributions All authors contributed to the study conception and design. Material preparation, data collection, and analysis were performed by Lin-Jun Hou, Peng Xu, and Zhi-Meng Hu. The first draft of the manuscript was written by Lin-Jun Hou, and all authors commented on the previous versions of the manuscript. All authors read and approved the final manuscript.

Data Availability The data that support the findings of this study are openly available in Science Data Bank at https://cstr.cn/31253.11.sciencedb.j00186.00742 and https://doi.org/10.57760/sciencedb.j00186.00742.

Declarations

Conflict of interest The authors declare that they have no conflict of interest.

References

1. Y.F. Guan, H.R. Yang, L.M. Duan et al., Measurement of fast neutrons with ^{238}U-coated fission chamber. Radiat. Detect. Technol. Methods **3**, 41 (2019). https://doi.org/10.1007/s41605-019-0115-1
2. Y.F. Guan, H.R. Yang, L.M. Duan et al., Comparison between experiment and simulation for the fission chamber used in fast neutron detection. Nucl. Phys. Rev. **36**, 4 (2019). https://doi.org/10.11804/NuclPhysRev.36.04.471
3. M. Li, Y.F. Guan, C.G. Lu et al., Measurement of TOF of fast neutrons with ^{238}U target. Nucl. Eng. Technol. **53**, 1964–1969 (2021). https://doi.org/10.1016/j.net.2020.12.003
4. Y. Jiang, J. Wu, Z. Li et al., A neutron beam monitor based on silicon carbide semiconductor coated with ^{6}LiF converter. Nucl. Instrum. Methods Phys. Res. Sect. A **921**, 14–17 (2019). https://doi.org/10.1016/j.nima.2018.12.014
5. A. Kargar, H.C. Hong, J. Tower et al., Thermal neutron detection with lithium-based semiconductors. Proc. SPIE 12241, Hard X-ray, Gamma Ray, and Neutron Detector Physics XXIV, 1224108 (2022). https://doi.org/10.1117/12.2632318
6. L.J. Ge, Z.M. Hu, Y.M. Zhang et al., Neutron emission spectroscopy measurements with a compact liquid scintillation detector for NBI-heated plasma at EAST. Plasma Phys. Controlled Fusion **60**, 095004 (2018). https://doi.org/10.1088/1361-6587/aad06c
7. Y.M. Zhang, L.J. Ge, J.Q. Sun et al., Velocity-space sensitivity of the compact neutron emission spectrometers at EAST. Rev. Sci. Instrum. **89**, 10I141 (2018). https://doi.org/10.1063/1.5039393
8. Z. Cui, Z. Hu, X. Xie et al., Assembling and testing of liquid scintillation detectors on the EAST neutron camera. J. Instrum. **14**, C05010 (2019). https://doi.org/10.1088/1748-0221/14/05/C05010

9. Y.Q. Zhang, L.Q. Hu, G.Q. Zhong et al., Development of a high-speed digital pulse signal acquisition and processing system based on MTCA for liquid scintillator neutron detector on EAST. Nucl. Sci. Tech. **34**, 150 (2023). https://doi.org/10.1007/s41365-023-01318-9
10. H. Ohgaki, I. Daito, H. Zen et al., Nondestructive inspection system for special nuclear material using inertial electrostatic confinement fusion neutrons and laser Compton scattering gamma-rays. IEEE Trans. Nucl. Sci. **64**, 1635–1640 (2017). https://doi.org/10.1109/TNS.2017.2652619
11. Q.H. Zhang, J.Q. Yang, X.S. Li et al., High order fast neutron multiplicity measurement equations based on liquid scintillation detector. Appl. Radiat. Isot. **152**, 45–51 (2019). https://doi.org/10.1016/j.apradiso.2019.06.022
12. J.B. Birks, *The Theory and Practice of Scintillation Counting* (Pergamon, Oxford, 1964), pp.185–234
13. S.X. Liu, W. Zhang, Z.H. Zhang et al., Performance of real-time neutron/gamma discrimination methods. Nucl. Sci. Tech. **34**, 8 (2023). https://doi.org/10.1007/s41365-022-01160-5
14. Y.H. Chen, X.M. Chen, X.D. Zhang et al., Study of n-γ discrimination in low energy range (above 40 keVee) by charge comparison method with a BC501A liquid scintillation detector. Chin. Phys. C **38**, 036001 (2014). https://doi.org/10.1088/1674-1137/38/3/036001
15. F.P. Wang, M.H. Yang, J.Y. Wang et al., A comparison of small-batch clustering and charge-comparison methods for n/γ discrimination using a liquid scintillation detector. Nucl. Instrum. Methods Phys. Res. Sect. A **1028**, 166379 (2022). https://doi.org/10.1016/j.nima.2022.166379
16. C.X. Zhang, S.T. Lin, J.L. Zhao et al., Discrimination of neutrons and γ-rays in liquid scintillator based on Elman neural network. Chin. Phys. C **40**, 086204 (2016). https://doi.org/10.1088/1674-1137/40/8/086204
17. H.R. Liu, Z. Zuo, P. Li et al., Anti-noise performance of the pulse coupled neural network applied in discrimination of neutron and gamma-ray. Nucl. Sci. Tech. **33**, 75 (2022). https://doi.org/10.1007/s41365-022-01054-6
18. Y.Q. Li, B.J. Zhu, Y. Lv et al., Artificial neural network algorithm for pulse shape discrimination in $2\pi\alpha$ and $2\pi\beta$ particle surface emission rate measurements. Nucl. Sci. Tech. **34**, 153 (2023). https://doi.org/10.1007/s41365-023-01305-0
19. A. Karmakar, A. Pal, G. Anil Kumar et al., Deep neural network-based pulse shape discrimination of neutrons and γ-rays in organic scintillation detectors. Pramana **97**, 157 (2023). https://doi.org/10.1007/s12043-023-02641-x
20. C. Fu, A. Di Fulvio, S.D. Clarke et al., Artificial neural network algorithms for pulse shape discrimination and recovery of piled-up pulses in organic scintillators. Ann. Nucl. Energy **120**, 410–421 (2018). https://doi.org/10.1016/j.anucene.2018.05.054
21. J. Kim, B. Jeon, J. Hwang et al., Pulse height estimation and pulse shape discrimination in pile-up neutron and gamma ray signals from an organic scintillation detector using multi-task learning. Appl. Radiat. Isot. **199**, 110880 (2023). https://doi.org/10.1016/j.apradiso.2023.110880
22. L.F. Liu, H. Shao, Study on neutron–gamma discrimination method based on the KPCA-GMM-ANN. Radiat. Phys. Chem. **203**, 110602 (2023). https://doi.org/10.1016/j.radphyschem.2022.110602
23. S.Y. Zhang, Z. Wei, P.Q. Zhang et al., Neutron-gamma discrimination with broaden the lower limit of energy threshold using BP neural network. Appl. Radiat. Isot. **205**, 111179 (2024). https://doi.org/10.1016/j.apradiso.2024.111179
24. S. Yoon, C. Lee, B.H. Won et al., Fast neutron-gamma discrimination in organic scintillators via convolution neural network. J. Korean Phys. Soc. **80**, 427–433 (2022). https://doi.org/10.1007/s40042-022-00398-x
25. K.P. Lennox, P. Rosenfield, B. Blair et al., Assessing and minimizing contamination in time of flight basedvalidation data. Nucl. Instrum. Methods Phys. Res. Sect. A **870**, 30–36 (2017). https://doi.org/10.1016/j.nima.2017.04.022
26. D. Fobar, L. Phillips, A. Wilhelm et al., Considerations for training an artificial neural network for particle type identification. IEEE Trans. Nucl. Sci. **68**, 2350–2357 (2021). https://doi.org/10.1109/TNS.2021.3103658
27. A. Hachem, Y. Moline, G. Corre et al., Labeling strategy to improve neutron/gamma discrimination with organic scintillator. Nucl. Eng. Technol. **55**, 4057–4065 (2023). https://doi.org/10.1016/j.net.2023.07.024
28. D.Z. Ding, C.T. Ye, Z.X. Zhao et al., *Neutron Physics: Principles, Methods and Applications* (Atomic Energy Press, Beijing, 2001), p.56
29. J.H. Kelley, J.E. Purcell, C.G. Sheu, Energy levels of the light nuclei A=12. Nucl. Phys. A **968**, 71–253 (2017). https://doi.org/10.1016/j.nuclphysa.2017.07.015
30. Z.Z. Liu, J.X. Chen, P. Zhu et al., Measurement of 4.438 MeV γ-ray to neutron intensity ratio for Am-Be neutron source. At. Energy Sci. Technol. (in Chinese) **42**(2), 300–304 (2008). https://doi.org/10.7538/yzk.2008.42.04.0300
31. A.R. Conn, N.I.M. Gould, P.L. Toint, *Trust Region Methods*. (Society for Industrial and Applied Mathematics, Philadelphia, 2000), pp. 749–777. https://doi.org/10.1137/1.9780898719857
32. S. Agostinelli, J. Allison, K. Amako et al., Geant4–a simulation toolkit. Nucl. Instrum. Methods Phys. Res. Sect. A **506**, 250–303 (2003). https://doi.org/10.1016/S0168-9002(03)01368-8
33. J. Allison, K. Amako, J. Apostolakis et al., Geant4 developments and applications. IEEE Trans. Nucl. Sci. **53**, 270–278 (2006). https://doi.org/10.1109/TNS.2006.869826
34. M. Asai, A. Dotti, M. Verderi et al., Recent developments in Geant4. Ann. Nucl. Energy **82**, 19–28 (2015). https://doi.org/10.1016/j.anucene.2014.08.021
35. J.C. Hopkins, G. Breit, The $^{1}\mathrm{H}(n,n)^{1}\mathrm{H}$ scattering observables required for high-precision fast-neutron measurements. At. Data Nucl. Data Tables **9**, 137–145 (1971). https://doi.org/10.1016/S0092-640X(71)80038-4
36. C. Szegedy, V. Vanhoucke, S. Ioffe et al., Rethinking the inception architecture for computer vision. Paper presented at the 2016 IEEE Conference on Computer Vision and Pattern Recognition (CVPR), Las Vegas, 27–30 June (2016). https://doi.org/10.1109/CVPR.2016.308
37. I. Sergey, S. Christian, Batch normalization: accelerating deep network training by reducing internal covariate shift. arXiv: 1502.03167 (2015). https://doi.org/10.48550/arXiv.1502.03167
38. N. Srivastava, G. Hinton, A. Krizhevsky et al., Dropout: a simple way to prevent neural networks from overfitting. J. Mach. Learn. Res. **15**, 1929–1958 (2014). http://jmlr.org/papers/v15/srivastava14a.html